

1 **Hydrodynamics, erosion and accretion of intertidal mudflats in**
2 **extremely shallow waters**

3

4 Benwei Shi ^{a, b*}, James R. Cooper ^c, Jiasheng Li ^d, Yang Yang ^a, S. L. Yang ^a, Feng Luo ^e, Zixian
5 Yu ^f, Ya Ping Wang ^{a, *}

6

7 ^a *State Key Laboratory of Estuarine and Coastal Research, East China Normal University,*
8 *Shanghai 200062, China*

9 ^b *State Key Laboratory of Marine Geology, Tongji University, Shanghai 200092, China.*

10 ^c *Department of Geography and Planning, School of Environmental Sciences, University of*
11 *Liverpool, Liverpool, UK.*

12 ^d *Ministry of Education Key Laboratory for Coast and Island Development, Nanjing University,*
13 *Nanjing 210093, China.*

14 ^e *Jiangsu Key Laboratory of Coast Ocean Resources Development and Environment Security,*
15 *Hohai University, Nanjing 210098, China*

16 ^f *Rudong Meteorology Bureau, Nantong, 226400, China.*

17 Corresponding author information,

18 Telephone: 086-25-83686010;

19 Fax: 086-25-83595387;

20 Email address: bwshi@sklec.ecnu.edu.cn (Benwei Shi)

21 ypwang@nju.edu.cn (Y. P. Wang).

22 **Abstract** Intertidal flats are shallow-water environments that undergo cyclical
23 variations in water depth, leading to a frequent occurrence of extremely shallow water
24 stages (ESWS; water depths $<0.2\text{m}$). However, relatively little is known about the
25 hydrodynamic conditions and erosion–accretion processes during ESWS, because the
26 water depth is too shallow to measure in situ sediment dynamic processes using
27 traditional methods. To address this gap, based on in situ measurements with four
28 advanced instruments, we quantified the hydrodynamic conditions, erosion and
29 accretion during ESWS in calm weather conditions on a highly turbid intertidal flat in
30 Jiangsu coast, China. Our results revealed that marked erosion and accretion occurred
31 during ESWS at the flood and ebb tidal stages, respectively. The resulting bed-level
32 changes were three times greater during ESWS than relatively deep water stages
33 (RDWS; water depths $>0.2\text{m}$), and the rate of change was an order of magnitude
34 faster than during RDWS. This larger and faster bed-level change occurred even
35 though the ESWS duration only accounted for 10% of the entire tidal cycle. This
36 result occurred because the bed shear stress due to combined current–wave action
37 during ESWS, was, on average, two times higher than during RDWS at the flood
38 stage causing more extensive erosion. Whereas during the ebb stage, this shear stress
39 during ESWS was only half of that during RDWS resulting in greater accretion. The
40 main implications of these results are that, because ESWS occur frequently (twice
41 every tide) and are associated with large bed shear stress and bed-level changes, these
42 conditions are likely to play an important role in morphological changes of intertidal
43 flats. Our study shows that ESWS have a key influence on intertidal flat

44 hydrodynamics and sediment dynamics. Thus our results are the basis for an improved
45 understanding of the coastal morphodynamic processes on intertidal flats.

46 **Keywords:** Extremely shallow water stages; Bed-level changes; Hydrodynamics;
47 Sediment transport.

48

49 **1. Introduction**

50 Intertidal flats are generally broad, shallowly sloping, intertidal zones with
51 fine-grained sedimentary deposits (Eisma, 1998). These flats are highly productive
52 components of shelf ecosystems (Le Hir *et al.*, 2000; Ysebaert *et al.*, 2003; Balke *et*
53 *al.*, 2011; Suykerbuyk *et al.*, 2016), supporting large numbers of invertebrates and fish
54 (Barbier, 2013; Bouma *et al.*, 2016), and playing a key role in recycling organic
55 matter and nutrients from both terrestrial and marine sources (Kautsky and Evans,
56 1987; Meziane and Tsuchiya, 2000; Li *et al.*, 2012). Thus, developing an in-depth
57 understanding of the processes that drive the dynamics of intertidal flats is important
58 for management strategies and engineer design. One particular area that requires
59 further investigation is the hydrodynamic and sediment transport processes that occur
60 during extremely shallow water stages (ESWS), defined in this study as stages of
61 water depth $(h) < 0.2\text{m}$.

62 Previous studies have focused primarily on relatively deep water stages (RDWS;
63 defined here as $h > 0.2\text{m}$), revealing that the non-linear interactions between waves
64 and currents on intertidal flats are responsible for strong turbulent mixing in the
65 bottom boundary layer (e.g., Dyer, 1989; Le Hir *et al.*, 2000; MacVean and Lacy,

66 2014; Yang *et al.*, 2016; Yu *et al.*, 2017), sediment transport in the tidal water column
67 (e.g., Janssen-Stelder, 2000; Wang *et al.*, 2012; Shi *et al.*, 2016), and morphological
68 evolution (e.g., Andersen *et al.*, 2006; Shi *et al.*, 2014; Hu *et al.*, 2015). However,
69 intertidal flats worldwide are predominately shallow-water environments. Flats
70 experience regular temporal–spatial variations in water depth due to cycles of
71 emergence and submergence, leading to the frequent occurrence of extremely shallow
72 water conditions (Gao, 2010; Fagherazzi and Mariotti, 2012; Zhang *et al.*, 2016). In
73 general, every tide has two ESWS, which are the initial stage of the flood tide and the
74 following ebb tide. In comparison with RDWS, the maximum or minimum suspended
75 sediment concentration (SSC) and current velocity within an entire tidal cycle may
76 occur during ESWS (Gao, 2010; Zhang *et al.*, 2016). Although this stage can be very
77 short (typically several minutes, but sometimes only several seconds) with an entire
78 tidal cycle (Gao, 2010), there is considerable potential for sediment trans-
79 port and erosion–accretion during ESWS (Downing *et al.*, 1981; Wang *et al.*, 2012; Shi *et al.*,
80 2017). Therefore, ESWS might play a significant role in controlling the overall
81 topography of intertidal flats (Fagherazzi and Mariotti, 2012). For example, ESWS
82 may promote the formation and destruction of micro-topography, such as sand ripples
83 and grooves (Zhang *et al.*, 2016), further resulting in the formation and modification
84 of larger geomorphic units (Zhou *et al.*, 2014).

85 Our understanding of the potentially important role of ESWS in the dynamics of
86 intertidal flats is limited, because field investigations of hydrodynamic and
87 erosion–accretion processes during ESWS are rare (e.g., Gao, 2010; Zhang *et al.*,

88 2016). The main reasons for this are twofold. First, the extensive field instrumentation
89 needed to gain integrated measurements of hydrodynamics, erosion–accretion, and
90 sediment transport processes during ESWS is technologically challenging (Williams
91 *et al.*, 2008; Fagherazzi and Mariotti, 2012; MacVean and Lacy, 2014). Sec-ondly,
92 there are few reliable numerical models for modeling sediment dynamic processes
93 during ESWS, due to difficulties in obtaining solvable equations for the complex
94 sediment exchange and strong turbulent mixing processes in these conditions.

95 Therefore, this paper examines how hydrodynamic conditions, SSCs, and bed
96 erosion–accretion processes differ between ESWS and RDWS on a highly turbid
97 intertidal flat off the Jiangsu coast, China. We present time-series field measurements
98 of current velocities, waves, SSCs, and bed-level changes throughout a number of
99 tidal cycles un-der calm weather conditions. These continuous measurements form the
100 basis for evaluating the link between hydrodynamics and bed-level changes during
101 ESWS. Our data provide new insights into the importance of ESWS in controlling bed
102 erosion–accretion processes and highlight that ESWS are critical in driving
103 morphological change on inter-tidal flats.

104

105 **2. Study area**

106 Our study site is located on the Rudong intertidal flat, Jiangsu coast, China. This area
107 comprises the largest radial-shaped tidal sand ridge sys-tem on the Chinese
108 continental shelf in the southwestern Yellow Sea (Fig. 1A). The study area is a
109 well-developed intertidal flat with a gentle slope (0.018%–0.022%) and width of

110 several kilometers in the sea-ward direction (Zhu *et al.*, 1986; Wang and Ke, 1997).
111 The intertidal flat is a macrotidal area with a semi-diurnal tide and mean tidal range of
112 3.9–5.5m (Ren *et al.*, 1985; Wang and Ke, 1997; Xing *et al.*, 2012). The flat is highly
113 turbid due to the abundant sediment supply from the Yangtze River and abandoned
114 Yellow River (Fig. 1A). The study area experiences frequent variations in water depth,
115 and ESWS occurs twice every tide and approximately four times each day. A small
116 wave height of <1m generally characterizes the study area during normal weather, and
117 the annual average wind speed is 4–5m/s (Ren, 1986). The inter-tidal area is generally
118 flat and has no obvious tidal creek near the study site (Fig. 1B). The surface sediments
119 are mainly silt (8–63 μ m) on the up-per tidal flat and fine sand (63–125 μ m) on the
120 middle tidal flat (Wang and Ke, 1997).

121

122 **3. Materials and methods**

123 **3.1 Field measurements**

124 **3.1.1 Data collection**

125 The field campaigns were conducted from November 28 to Decem-ber 2, 2016.
126 All instruments were installed firmly on a custom-made frame with an open structure
127 and two stainless steel legs (Fig. 2). The relative height above the bed and setup of the
128 instruments are detailed in Fig. 2 and Table 1, respectively.

129

130 Near-bed turbulent boundary velocities were measured using a

131 downward-looking 6MHz Nortek acoustic Doppler velocimeter (ADV) (measurement
132 accuracy of ± 1 mm/s; data output rate of 1–64Hz) at a sampling frequency of 16Hz in
133 5min bursts (4096 points per 5min time-series). The ADV was fastened to the
134 custom-made frame with the probe head positioned 0.2m above the bed (Table 1), and
135 measured the 3D turbulent velocity at a standoff distance of just 0.15m from the probe
136 head (Fig. 2). Thus, the turbulent velocities were measured at a height of ~ 0.05 m
137 above the bed surface. To measure the turbulent velocity, the probe must be
138 submerged, meaning that measurements of current velocities could only be
139 undertaken when the water depth was >0.2 m (i.e., not during ESWS). In addition to
140 measuring the turbulent velocity, the ADV probe recorded a time-series of distance
141 (with an accuracy of ± 1 mm) between the probe head and the local bed surface at 1Hz.
142 As such, actual bed elevation changes could be extracted from the time-series
143 (Andersen *et al.*, 2007; Salehi and Strom, 2012). The accuracy of the ADV
144 measurements is robust and has been tested extensively in the laboratory (Salehi and
145 Strom, 2012) and in the field (Andersen *et al.*, 2007; Wang *et al.*, 2014; Shi *et al.*,
146 2015).

147 To capture the current velocity during ESWS, an electromagnetic current meter
148 (EMCM) was used because this instrument is not affected by blind measurement areas,
149 has a very small measurement volume, and a small probe diameter (~ 3 cm). To
150 measure the 2D current velocity as close to the bed as possible, the EMCM was
151 deployed at a height of only 0.05m above the bed and operated at a burst period of 30s
152 and sampling frequency of 2Hz (Fig. 2; Table 1).

153 Wave height was measured at a sampling frequency of 4Hz over a 256s period
154 using a SBE 26plus SEAGAUGE (Wave and Tide Recorder; accuracy of 0.01% of the
155 full scale) (Table 1). The SBE 26plus was installed horizontally on the bed, and its
156 pressure sensor was located 0.05cm above the bed (i.e., as close to the bed as possible)
157 to record waves during ESWS (Fig. 2). The SBE 26plus collected 1024
158 measurements per burst and the mean water level was obtained every 10min (Table
159 1). On the intertidal flat, the wave period was generally 2–5s, and thus each burst
160 recorded >100 waves for estimation of wave height and period.

161 An optical backscattering sensor (OBS-3A; self-recording turbidity–temperature
162 monitoring instrument) was used to make in situ measurements of turbidity at a
163 sampling frequency of 1Hz, with its sensor facing outward at a height of 0.05m above
164 the bed (Table 1; Fig. 2). To calibrate the in situ turbidity measurements in the
165 laboratory, *in situ* water samples were collected at the same height as the OBS-3A
166 measurements on a small boat near the observation sites.

167

168 **3.1.2 Determination of ESWS duration and bed-level changes**

169 The ADV probes were exposed to air and stopped working when the water depth
170 was < 0.2 m. Thus, the ADV instrument could not record the time at which the water
171 attained a zero depth or the distance between the ADV probe and bed surface at this
172 time. Therefore a boat anchored near the observation site recorded this time using a
173 watch and the distance using a ruler. For the initial stage of flood tide, the duration
174 (ΔT_{F-i}) and bed-level change (ΔD_{F-i}) of ESWS for each tide were estimated as

175 follows:

176

$$177 \quad \Delta T_{F-i} = T_{F-i} - T_{f-b-i} \quad (1)$$

$$178 \quad \Delta D_{F-i} = D_{F-i} - D_{f-b-i} \quad (2)$$

179

180 where T_{F-i} and D_{F-i} are the time and distance, respectively, recorded when the water
181 attained a zero depth at the initial stage of flood tide i , and T_{f-b-i} and D_{f-b-i} are the time
182 and distance, respectively, recorded by the ADV at the first effective burst when $h \geq$
183 0.2 m during the flood tide stage.

184 For the post-ebb tide stage, the duration (ΔT_{E-i}) and bed-level change (ΔD_{E-i}) of
185 ESWS for each tide were estimated as follows:

186

$$187 \quad \Delta T_{E-i} = T_{e-b-i} - T_{E-i} \quad (3)$$

$$188 \quad \Delta D_{E-i} = D_{e-b-i} - D_{E-i} \quad (4)$$

189

190 where T_{e-b-i} and D_{e-b-i} are the time and distance, respectively, recorded by the ADV in
191 the last effective burst during the ebb stage during tide i (i.e., when $h \approx 0.2$ m), and
192 T_{E-i} and D_{E-i} are the time and distance, respectively, recorded when the water attained
193 a zero depth at the post-ebb tide stage during tide i .

194

195 **3.2 Estimation of bed shear stress**

196 The variation in bed shear stress within an entire tidal cycle was estimated using

197 a current–wave interaction model. Specifically, the bed shear stress due to waves (τ_w)
198 was calculated using the theory of wave orbital velocity (A1 in Appendix A) and wave
199 friction (A3 and A4 in Appendix A), and the bed shear stress due to currents (τ_c) was
200 calculated using the theory of bottom boundary layers (A5 and A6 in Appendix A) and
201 friction velocity (u_*). The bed shear stress due to combined current–wave action (τ_{cw})
202 was calculated using the Grant and Madsen (1979) model (a classic current–wave
203 interaction model; A7 in Appendix A), which has been widely used in the estimation
204 of τ_{cw} (e.g., Lyne *et al.*, 1990; Mellor, 2002; Feddersen *et al.*, 2003; Zhang *et al.*,
205 2004).

206 The bottom sediments were mainly very fine sand. At study site A the median
207 grain size (d_{50}) was 113 μm during the field measurements. Thus, we determined the
208 critical shear stress for erosion (τ_{cr}) using the Shields (1936) equation (B3, B4, and B5
209 in Appendix B), which has been applied by Miller *et al.* (1977), Soulsby (1997), and
210 Yang *et al.* (2016a). In this study, we used a value of 0.1 N/m^2 based on this median
211 grain size.

212

213 **4. Results**

214 **4.1 Wind, wave, and current data**

215 During field measurements, offshore winds ranged in speed from 0.6 to 7.5 m/s,
216 with a mean of 3.5 m/s (Fig. 3A), which was weaker than the annual mean wind speed
217 of 4–5 m/s (Ren, 1986). Relatively weak winds generated small waves during the field
218 measurements. Thus, the maximum wave height was just 0.39 m (Fig. 3B). Wave

219 height within an entire tidal cycle tended to be largest at the high water level and
220 smallest at the low water level (Fig. 3B). The wave height was at its minimum during
221 ESWS (Fig. 3B), perhaps due to the positive relationship between wave height and
222 water depth.

223 Wave period and water depth showed the same temporal pattern. The maximum
224 wave period was only 4.3 s, which tended to occur at high water levels, and the
225 minimum (~1 s) occurred at ESWS during each tide (Fig. 3B–C).

226 Current velocity was rotational for the entire tidal cycle (Fig. 3D). The maximum
227 current velocity occurred during ESWS in the initial flood stage (0.1–0.59 m/s), in an
228 onshore direction (towards the south), and was greater than the current velocity during
229 ESWS in the post-flood stage when the current direction switched to offshore (Fig.
230 3D). The current during RDWS tended to have an onshore direction in the flood stage,
231 offshore direction in the ebb stage, and a smaller velocity than during ESWS in the
232 initial flood stage (Fig. 3D).

233

234 **4.2 Bed shear stresses**

235 **4.2.1 Shear stress due to waves (τ_w) and currents (τ_c)**

236 The τ_w values varied little within a tidal cycle (0.01–0.15 N/m²; Fig. 4B; Table 2)
237 as a result of weak winds and small wave heights (Fig. 3B) under the calm weather
238 conditions. The τ_w values during ESWS were comparable with those during RDWS
239 (Table 2). The maximum τ_c value occurred during ESWS in the flood stage (Fig. 4B).
240 The average τ_c during ESWS in the flood stage (0.30–0.64 N/m²) was several times

241 greater than during ESWS at the corresponding ebb stage (0.07–0.16 N/m²), and was
242 also greater than the average value during a RDWS in a corresponding tide (0.11–0.13
243 N/m²) (Table 2).

244

245 **4.2.2 Shear stress due to combined current–wave action (τ_{cw})**

246 The maximum τ_{cw} value within a tidal cycle occurred during ESWS in the flood
247 stage (Fig. 4B), and the average τ_{cw} during these stages ranged from 0.36 to 0.70 N/m²
248 and was greater than τ_{cr} (0.1 N/m²). In contrast, the average τ_{cw} during ESWS at the
249 corresponding ebb stage ranged from 0.03 to 0.09 N/m² and was less than the average
250 τ_{cr} (Fig. 4B). For RDWS, the average τ_{cw} varied little, ranging from 0.12 to 0.14 N/m²,
251 and was slightly greater than the average τ_{cr} .

252

253 **4.3 Suspended sediment concentration**

254 The average SSC during ESWS at the flooding stage (0.69 kg/m³) was two times
255 higher than at the ebb stage (0.33 kg/m³; Table 2; Fig.4C). In contrast, the average
256 SSC during RDWS was lower than during ESWS at the corresponding flood stage and
257 was higher than at the corresponding ebb stage (Table 2; Fig.4C).

258

259 **4.4 Duration of ESWS and RDWS**

260 The duration of ESWS at the ebb stage (~30 min) was 1.5 times longer than that
261 at the corresponding flood stage (~22 min), and the duration of ESWS only accounted
262 for 10% of the entire tidal cycle (Table 3). In contrast, the duration of RDWS was 457

263 min on average, which was almost nine times longer than the average total duration
264 (52 min) of ESWS. Thus, RDWS accounted for 90% of the entire tidal cycle (Table
265 3).

266

267 **4.5 Bed-level changes**

268 During the entire field campaign the distance from the ADV probe to the bed
269 surface ranged from 280 to 285 mm, indicating that the overall bed-level change was
270 just -5 mm (negative denoting erosion) (Fig. 4D). The bed-level change during ESWS
271 was much greater than that during RDWS (Table 3; Fig. 4D). Erosion occurred during
272 ESWS at the flooding stage of the tide, with an average magnitude of -7.4 mm (-4.2
273 to -10.3 mm) per tide at an average rate of -0.4 mm/min (-0.2 to -0.5 mm/min; Table
274 3). In contrast, accretion occurred during ESWS in the ebb stage, and the rate of this
275 accretion was comparable to that of erosion, with the average amount being $+9.2$ mm
276 ($+4.4$ to $+14.5$ mm; positive denoting accretion) per tide at an average rate of $+0.3$
277 mm/min ($+0.1$ to $+0.5$ mm/min; Table 3). However the rate of bed-level change for
278 RDWS was much lower, with an average amount of -2.5 mm ($+3.5$ to -7.0 mm) per
279 tide at an average rate of -0.6×10^{-2} mm/min ($+1 \times 10^{-2}$ to -2×10^{-2} mm/min; Table
280 3). Therefore, the magnitude of bed-level change during ESWS was three times
281 greater than that during RDWS, and its rate was an order of magnitude higher, despite
282 ESWS making up just 10% of the tidal cycle (Table 3).

283

284 **5. Discussion**

285 Our results reveal that strong erosion and weak accretion occurred during ESWS
286 at the flood and ebb stages of a tide, respectively, and relatively weak erosion
287 occurred during RDWS in almost all tidal cycles (Table 3; Fig. 4D). This difference
288 can be explained by the theory of sediment erosion–accretion (Appendix B;
289 Winterwerp and van Kesteren, 2004) and the contrast in bed shear stress between
290 ESWS and RDWS. The average erosion flux (F_e) during ESWS in the flood stage was
291 greater than that during RDWS because the average τ_{cw} during ESWS in the flood
292 stage was two times higher than during RDWS in a corresponding tidal cycle (Table 2;
293 Fig. 4B) and greater than τ_{cr} . In contrast, in the ebb stage, the average F_e during
294 ESWS was zero (due to $\tau_{cw} < \tau_{cr}$) and the average depositional flux (F_d) was much
295 greater than during RDWS, because the average τ_{cw} during ESWS was only half of the
296 average τ_{cw} during RDWS (Table 2; Fig. 4B). The τ_{cw} values were much lower than τ_{cr}
297 values during ESWS, resulting in greater accretion. This accretion occurred during
298 periods of much higher near-bed SSCs than were observed during RDWS (Table 2),
299 reflecting relatively weak hydrodynamic conditions.

300 A detailed comparison of the bed-level changes and durations of ESWS and
301 RDWS showed that ESWS were characterized by much shorter duration (10% of the
302 entire tidal cycle), and larger and faster bed-level changes (Table 3). Morphological
303 changes are generally related to not only the magnitude of extreme events, but also the
304 frequency of their occurrence (Wolman and Miller, 1960). Thus, when considering the
305 effects of ESWS on geomorphic processes on the studied intertidal flat, we should
306 note that, although short in duration, ESWS occur twice every tidal cycle and there

307 are two daily tidal cycles at this site (e.g., Wang *et al.*, 2012; Xing *et al.*, 2012).
308 Therefore, ESWS occurs frequently on the intertidal flat. Given this high frequency
309 and that ESWS are marked by large values of bed shear stress, these conditions have
310 an important influence on the morphological development of intertidal flats. To
311 illustrate this, we estimated the annual net cumulative bed-level change induced by
312 ESWS to be about +66cm, whereas this is about -182cm during RDWS. Therefore,
313 ESWS play a significant role in the annual replenishment of sediments. Given that our
314 field investigations were undertaken in calm weather conditions, we can infer that in
315 rough or stormy weather conditions the magnitude of bed-level changes during ESWS
316 could be even larger.

317 It is important to consider whether our results are site-specific or are applicable
318 to other intertidal environments. Based on a limited number of previous studies, we
319 suggest the latter is the case for the following reason. Surges or pulses in tidal velocity
320 have been identified in association with high SSCs in ESWS in different types of
321 intertidal flats, such as: (i) sandy and muddy coasts (e.g., Postma, 1967;
322 Bayliss-Smith *et al.*, 1979; Gao, 2010; Nowacki and Ogston, 2013; Zhang *et al.*,
323 2016); (ii) different geomorphic units within intertidal systems, such as tidal creeks
324 and runnels (Fagherazzi *et al.*, 2008; Fagherazzi and Mariotti, 2012; Hughes, 2012);
325 (iii) in a range of intertidal systems, such as channel-flat and salt marsh systems
326 (Pethick, 1980; Wang *et al.*, 1999; Nowacki and Ogston, 2013); and (iv) under a range
327 of meteorological conditions, including calm and stormy weather (Wang *et al.*, 1999;
328 Zhang *et al.*, 2016). These observations suggest that this velocity surging/pulsing is

329 common during ESWS in almost all tidal cycles in intertidal environments worldwide.
330 Furthermore, based on the results of Zhang *et al.* (2016), these surges can produce
331 large bed shear stress (up to 1.5N/m^2) at the beginning of the flood tide, which is an
332 order of magnitude higher than the critical shear stress of sediments commonly found
333 on intertidal flats. Therefore, it is reasonable to expect that this surge could re-suspend
334 and transport a large amount of bottom sediment, resulting in erosion at the beginning
335 of the flood tide. This inference is in agreement with the strong erosion observed
336 during ESWS in our study.

337 Previous studies have been conducted on field measurement of ESWS (Zhang *et al.*
338 *al.*, 2016; Shi *et al.*, 2017). For example, Shi *et al.* (2017) have estimated the
339 bed-level changes of ESWS during windy weather conditions on the same intertidal
340 flat as this study, but on a different section. Their results have showed that bed-level
341 changes due to erosion under calm conditions were six times lower than those
342 reported in Shi *et al.* (2017) (-14.7mm in Shi *et al.* (2017) vs. -2.3mm (this study))
343 while bed-level changes due to accretion was slightly higher under our calm
344 conditions ($+6.8\text{mm}$ (this study) vs. $+5.1\text{mm}$ in Shi *et al.* (2017)). The reason is that
345 this study was made under calm conditions, which representing a rather weak
346 intertidal sediment dynamics, while the results in Shi *et al.* (2017) represented relative
347 stronger hydrodynamics since the wind speed could reached up to 13.6 m/s (Shi *et al.*,
348 2017), showing that weather conditions can be an important factor in determining the
349 importance of ESWS in morphological changes.

350 The limitations of this study are that we lacked the field data needed to measure

351 in big detail time series of bed-level change to study processes and mechanism of
352 sediment erosion, accretion, transport, biogeochemical cycle and micro-topography
353 formation during ESWS. Therefore, the further avenues of research on sedimentary
354 processes and hydrodynamics during ESWS should focus on the following: (1) spatial
355 comparisons of sediment transport processes during ESWS in the sub-tidal, middle,
356 and high intertidal zones. Hydrodynamics in these zones may differ greatly during
357 ESWS compared with other periods, driving morphological change; (2) a comparison
358 of sedimentary processes during ESWS in microtidal, mesotidal, and macrotidal
359 intertidal flats, sheltered and exposed intertidal flats, and under calm and stormy
360 weather conditions. For example, our study was performed under weak wind
361 conditions, and there will likely be a difference in sedimentary processes under rough
362 or storm weather conditions. (3) investigation of the interactions between
363 hydrodynamics and micro-topography (e.g., ripples). Micro-topography formation and
364 destruction are common during ESWS (Zhang *et al.*, 2016). This micro-topography
365 can greatly increase bottom friction (Ke *et al.*, 1994), which can slow current
366 velocities and tidal wave propagation (Friedrichs and Madsen, 1992; Le Hir *et al.*,
367 2000). Thus this enhanced bottom friction could increase turbulence within the
368 near-bed region (Nezu and Nakagawa, 1993) and possibly bed-level change.
369 Therefore, there is a need to undertake integrated and high-resolution measurements
370 of currents, waves, SSCs, bed-level changes, and micro-topography during ESWS to
371 better understand their interactions. (4) smaller instrument measurement volumes and
372 standoff distances are required to facilitate in situ measurements in extremely

373 shallow-water environments to allow improved parameterization of turbulence and
374 sediment transport. (5) examination of the effects of sediment transport processes
375 during ESWS on biogeochemical cycling. ESWS are usually characterized by high
376 SSCs (Gao, 2010), which are rich in trace metals, nutrients, organic carbon, and
377 anthropogenic contaminants (Dyer *et al.*, 2000; Grabowski *et al.*, 2011). Thus, such
378 large and frequent erosion and accretion during ESWS are likely to play an important
379 role in biogeochemical cycling.

380

381

382 **6. Conclusions**

383 Integrated field measurements of current velocities, waves, SSCs, and bed-level
384 changes on an intertidal flat have quantified the hydrodynamic and sediment
385 erosion–accretion processes during ESWS close to the seabed. Our major findings and
386 their implications are as follows.

387 (1) The τ_{cw} values during ESWS in the initial flood stage were greater than the τ_{cr}
388 values, and the τ_{cw} values during ESWS in the post-ebb stage were less than
389 the τ_{cr} values. These differences in hydrodynamics led to strong erosion and
390 accretion during ESWS in the flood and ebb stage of a tide, respectively.
391 Relatively weak erosion occurred during RDWS in almost all tidal cycles.
392 This indicated a large difference in sediment dynamics between ESWS and
393 RDWS.

394 (2) Bed-level changes during ESWS were three times greater than during RDWS
395 in a corresponding tide, and the rate of change was an order of magnitude
396 higher than during RDWS. These larger and more rapid changes occurred
397 because τ_{cw} values during ESWS were, on average, two times higher than
398 during RDWS at the flood stage, and at the ebb stage τ_{cw} values were just half
399 of the average τ_{cw} value during RDWS. These bed-level changes occurred even
400 though ESWS made up only 10% of the entire tidal cycle.

401 (3) ESWS occur twice in every tide. Given that large bed shear stresses and
402 bed-level changes were associated with ESWS, this indicated that ESWS has
403 an important influence on morphological changes on intertidal flats.

404 (4) Our results demonstrated that ESWS have an important control on near-bed
405 hydrodynamics that influence sediment dynamics and morphological changes.
406 Thus further investigations into the relationships between hydrodynamics,
407 micro-topography, and sediment transport processes during ESWS under a
408 range of conditions will be an important area of future research for estuarine
409 scientists.

410

411 **Appendix A: Calculation of bottom shear stress**

412 The wave orbital velocity \hat{U}_δ [m/s] at the edge of the wave boundary layer was
413 estimated from the following equation:

414

$$415 \quad \hat{U}_\delta = \frac{\pi H}{T \sinh(2\pi h/L)} \quad (\text{A1})$$

416

417 where H is the wave height [m], T is the wave period [s], $L [= (gT^2/\pi) \tanh(2\pi h/L)]$ is
418 the wavelength [m], g is the acceleration due to gravity [9.81 m/s²], and h is the water
419 depth [m].

420 The wave-related bottom shear stress τ_w [N/m²] was estimated as follows (van
421 Rijn, 1993):

422

$$423 \quad \tau_w = \frac{1}{2} \rho_w f_{wr} \hat{U}_\delta^2 \quad (\text{A2})$$

424

425 where ρ_w is seawater density [1028 kg/m³] and f_{wr} is the wave friction coefficient [-],
426 which was calculated as follows (Soulsby, 1997):

$$427 \quad f_{wr} = 0.237 r^{-0.52} \quad (\text{A3})$$

$$428 \quad r = A/k_s \quad (\text{A4})$$

429 where r is the relative roughness [-], A is the semi-orbital excursion ($= \hat{U}_\delta T / 2\pi$ [m]),
430 and k_s is the Nikuradse grain roughness ($2.5 d_{50}$ [m]; d_{50} is the median grain size;
431 Whitehouse *et al.*, 2000).

432 During calm weather, the velocity structure in the bottom boundary layer is
433 considered to exhibit a logarithmic velocity profile (LP method) (e.g., Soulsby and

434 Dyer, 1981; Dyer, 1986; Grant and Madsen, 1986; Andersen *et al.*, 2007; Salehi and
435 Strom, 2012; Zhang *et al.*, 2016a, b) and is expressed as follows (Dyer, 1986;
436 Whitehouse *et al.*, 2000):

437

$$438 \quad u = \frac{u_*}{k} \ln \left(\frac{z}{z_0} \right) \quad (\text{A5})$$

439

440 where u is the measured velocity at height z above the bed [m/s], k is the von
441 Karman's constant (0.4) [-], z_0 is the bed roughness length related to the Nikuradse
442 grain roughness k_s ($z_0 = k_s/30$ [m]; Whitehouse *et al.*, 2000), and u_* is the friction
443 velocity [m/s]. Variation in u during ESWS was obtained from the EMCM instrument,
444 and variation in u during RDWS was obtained from the ADV instrument.

445 The current-related bottom shear stress τ_c [N/m²] was estimated from the friction
446 velocity u_* :

447

$$448 \quad \tau_c = \rho_w u_*^2 \quad (\text{A6})$$

449

450 where ρ_w is the density of seawater [kg/m³].

451 We used the current–wave interaction model (Grant and Madsen, 1979) to
452 calculate the bed shear stress due to combined current–wave action (τ_{cw}), which is
453 described as follows:

454

$$455 \quad \tau_{cw} = \sqrt{(\tau_w + \tau_c |\cos \varphi_{cw}|)^2 + (\tau_c \sin \varphi_{cw})^2} \quad (A7)$$

456

457 where φ_{cw} [°] is the angle between the wave and current directions. The current
 458 direction was obtained from the ADV and EMCM instruments. The wave direction
 459 was estimated by a standard PUV method (available at
 460 <http://www.nortekusa.com/usa/knowledge-center/table-of-contents/waves>). We
 461 computed wave directional spectra from ADV data by combining horizontal velocities
 462 and pressure data from the ADV data.

463

464 **Appendix B: Theory of sediment erosion and accretion**

465 Intratidal erosion and accretion typically depend on the balance between
 466 erosional F_e [kg/m²/s] and depositional flux F_d [kg/m²/s] (Winterwerp and van
 467 Kesteren, 2004; Lumborg, 2005). Net erosion occurs when $F_e > F_d$, and net accretion
 468 when $F_e < F_d$. Based on the work of Partheniades (1965) and Winterwerp and van
 469 Kesteren_(2004), erosional and depositional fluxes can respectively be expressed as
 470 follows (Owen, 1977; Whitehouse *et al.*, 2000):

471

$$472 \quad F_e = \begin{cases} M_e (\tau_{cw} - \tau_{cr}), & \tau_{cw} > \tau_{cr} \\ 0, & \tau_{cw} \leq \tau_{cr} \end{cases} \quad (B1)$$

$$473 \quad F_d = (\text{SSC}) w_{50} \quad (B2)$$

474

475 where τ_{cw} is the combined bed shear stress due to current–wave action [N/m^2], M_e is
476 the erodibility parameter [m/Pa/s] known as the erosion constant, SSC is the near-bed
477 concentration of suspended sediment [kg/m^3], w_{50} is the median settling velocity of
478 suspended sediment in the water column [m/s], and τ_{cr} is the critical bed shear stress
479 for erosion [N/m^2] obtained using the approach developed by Shields (1936), Miller *et*
480 *al.* (1977), and Soulsby (1997):

481

$$482 \quad \tau_{cr} = \theta_{cr} g (\rho_s - \rho_w) d_{50} \quad (\text{B3})$$

$$483 \quad \theta_{cr} = \frac{0.30}{1 + 1.2 D_*} + 0.055 [1 - \exp(-0.02 D_*)] \quad (\text{B4})$$

$$484 \quad D_* = \left[\frac{g(s-1)}{v^2} \right]^{\frac{1}{3}} d_{50} \quad (\text{B5})$$

485

486 where θ_{cr} is the threshold Shields parameter [-], ρ_s is the grain density [2650 kg/m^3],
487 D_* is the dimensionless grain size [-], s (ρ_s/ρ_w) is the ratio of grain density to seawater
488 density [2.58], and v is the kinematic viscosity of seawater [$1.36 \times 10^{-6} \text{ m}^2/\text{s}$].

489

490 **Acknowledgements**

491 We thank Dezhi Chen and Qingguang Zhu for their help with the fieldwork on
492 the Rudong intertidal flat in the Jiangsu coast, China. Special thanks are extended to

493 Chunyan Li for their helpful suggestions during the preparation of this manuscript.
494 This work was supported by the Natural Science Foundation of China (Grant numbers
495 41576090 and 41625021), the Jiangsu Special Program for Science and Technology
496 Innovation (HY2017-2), and State Key Laboratory of Marine Geology, Tongji
497 University (No. MG201906).

498 **References**

- 499 Andersen, T. J., Pejrup, M., Nielsen, A.A. 2006. Long-term and high resolution measurements
500 of bed level changes in a temperate, microtidal coastal lagoon. *Marine Geology*, 226,
501 115–125.
- 502 Andersen, T. J., J. Fredsoe, M. Pejrup (2007), In situ estimation of erosion and deposition
503 thresholds by Acoustic Doppler Velocimeter (ADV), *Estuarine Coastal Shelf Sci.*, 75,
504 327-336, doi: 10.1016/j.ecss.2007.04.039.
- 505 Balke, T., Bouma, T. J., Horstman, E. M., Webb, E. L., Erfemeijer, P. L., Herman, P. M. (2011).
506 Windows of opportunity: thresholds to mangrove seedling establishment on tidal flats.
507 *Marine Ecology Progress Series*, 440, 1-9.
- 508 Barbier, E. B. (2013). Valuing ecosystem services for coastal wetland protection and restoration:
509 Progress and challenges. *Resources*, 2, 213–230.
- 510 Bayliss-Smith TP, Healey R, Lailey R, Spencer T, Stoddart DR. 1979. Tidal flows in salt marsh
511 creeks. *Estuarine and Coastal Marine Science* 9(3), 235-55.
- 512 Bouma, T. J., van Belzen, J., Balke, T., van Dalen, J., Klaassen, P., Hartog, A. M., Herman, P. M.
513 J. (2016). Short-term mudflat dynamics drive long-term cyclic salt marsh dynamics.
514 *Limnology and Oceanography*, 61(6), 2261-2275.

515 Downing, J. P., Sternberg, R. W., Lister, C. R. B. (1981). New instrumentation for the
516 investigation of sediment suspension processes in the shallow marine environment. *Marine*
517 *Geology*, 42(1-4), 19-34.

518 Dyer, K.R., 1986. *Coastal and Estuarine Sediment Dynamics*. John Wiley and Sons.

519 Dyer, K.R. 1989. Sediment processes in estuaries: future research requirements. *Journal of*
520 *Geophysical Research*, 94 (C10), 14,327-14,339.

521 Dyer, K. R., M. C. Christie, N. Feates, M. J. Fennessy, M. Pejrup, and W. van der Lee (2000), An
522 investigation into processes influencing the morphodynamics of an intertidal mudflat, the
523 Dollard estuary, the Netherlands: I. Hydrodynamics and suspended sediment, *Estuarine*
524 *Coastal Shelf Sci.*, 50(5), 607–625, doi:10.1006/ecss.1999.0596.

525 Eisma, D. (1998), *Intertidal Deposits: River Mouth, Tidal Flats, and Coastal Lagoons*, CRC Press,
526 459 pp.

527 Fagherazzi, S., Hannon, M., D' Odorico, P. (2008). Geomorphic structure of tidal hydrodynamics
528 in salt marsh creeks. *Water resources research*, 44(2).

529 Fagherazzi, S., Mariotti, G. (2012). Mudflat runnels: Evidence and importance of very shallow
530 flows in intertidal morphodynamics. *Geophysical Research Letters*, 39(14) , L14402.

531 Feddersen, F., Gallagher, E. L., Guza, R. T., Elgar, S. (2003). The drag coefficient, bottom
532 roughness, and wave-breaking in the nearshore. *Coastal Engineering*, 48(3), 189-195.

533 Friedrichs, C. T., Madsen, O. S. (1992). Nonlinear diffusion of the tidal signal in frictionally
534 dominated embayments. *Journal of Geophysical Research: Oceans*, 97(C4), 5637-5650.

535 Gao, S. 2010. Extremely Shallow Water Benthic Boundary Layer Processes and the Resultant
536 Sedimentological and Morphological Characteristics. *Acta Sedimentologica Sinica*, 28(5):

537 926-932 (in Chinese).

538 Grabowski, R. C., Droppo, I. G., Wharton, G. (2011). Erodibility of cohesive sediment: the
539 importance of sediment properties. *Earth-Science Reviews*, 105(3), 101-120.

540 Grant, W. D., & Madsen, O. S. (1979). Combined wave and current interaction with a rough
541 bottom. *Journal of Geophysical Research*, 84, 1797–1808.

542 Grant, W.D., Madsen, O.S., 1986. The continental-shelf bottom boundary layer. *Annual Review*
543 *of Fluid Mechanics* 18 (1), 265–305.

544 Hu, Z., Z. B. Wang, T. J. Zitman, M. J. F. Stive, and T. J. Bouma (2015), Predicting long-term and
545 short-term tidal flat morphodynamics using a dynamic equilibrium theory, *J. Geophys. Res.*
546 *Earth Surf.*, 120, 1803–1823, doi:10.1002/2015JF003486.

547 Hughes, Z. J. (2012). Tidal channels on tidal flats and marshes. In *Principles of Tidal*
548 *Sedimentology*. Springer Netherlands, pp. 269-300

549 Janssen-Stelder, B. 2000. The effect of different hydrodynamic conditions on the
550 morphodynamics of a tidal mudflat in the Dutch Wadden Sea. *Continental Shelf Research*, 20,
551 1461-1478.

552 Kautsky, N., Evans, S. (1987). Role of biodeposition by *Mytilus edulis* in the circulation of matter
553 and nutrients in a Baltic coastal ecosystem. *Marine Ecology Progress Series*, 201-212.

554 Ke, X. K., M. B. Collins, and S. E. Poulos (1994), Velocity structure and sea-bed roughness
555 associated with intertidal (sand and mud) flats and salt-marshes of the Wash, UK, *Journal of*
556 *Coastal Research*, 10(3), 702–715.

557 Le Hir, P., W. Roberts, O. Cazaillet, M. Christie, P. Bassoullet, C. Bacher (2000), Characterization
558 of intertidal flat hydrodynamics, *Cont. Shelf Res.*, 20, 1433-1459.

559 Li, P., Yang, S.L., Milliman, J.D., Xu, K.H., Qin, W.H., Wu, C.S. 2012. Spatial, temporal, and
560 human-induced variations in suspended sediment concentration in the surface waters of the
561 Yangtze Estuary and adjacent coastal areas. *Estuaries Coasts* 35, 1316–1327.

562 Lumborg, U. 2005. Modelling the deposition, erosion, and flux of cohesive sediment through
563 Øresund. *Journal of Marine Systems*, 56(1), 179-193.

564 Lyne, V. D., Butman, B., Grant, W. D. (1990). Sediment movement along the US east coast
565 continental shelf—I. Estimates of bottom stress using the Grant-Madsen model and
566 near-bottom wave and current measurements. *Continental Shelf Research*, 10(5), 397-428.

567 MacVean, L. J., and J. R. Lacy (2014), Interactions between waves, sediment, and turbulence on a
568 shallow estuarine mudflat, *J. Geophys. Res. Oceans*, 119, 1534-1553,
569 doi:10.1002/2013JC009477.

570 Mellor, G. (2002). Oscillatory bottom boundary layers. *Journal of Physical Oceanography*, 32(11),
571 3075-3088.

572 Meziane, T., Tsuchiya, M. (2000). Fatty acids as tracers of organic matter in the sediment and food
573 web of a mangrove/intertidal flat ecosystem, Okinawa, Japan. *Marine Ecology Progress*
574 *Series*, 49-57.

575 Miller, M.C., McCave, I.N., Komar, P.D., 1977. Threshold of sediment motion under
576 unidirectional current. *Sedimentology*, 24, 507-527.

577 Nezu, I., Nakagawa, H. 1993. *Turbulence in Open Channel Flows*. IAHR Monograph, A. A.
578 Balkema, Rotterdam.

579 Nowacki, D. J., Ogston, A. S. (2013). Water and sediment transport of channel-flat systems in a
580 mesotidal mudflat: Willapa Bay, Washington. *Continental Shelf Research*, 60, S111-S124.

581 Owen, M.W. 1977. Problems in the modelling of transport, erosion, and deposition of cohesive
582 sediments. In: The ideas and observations on progress in the study of the seas, Vol.6, Ch. 12,
583 ed., Goldberg, E.D., 515-537. John Wiley and Sons Ltd.

584 Partheniades, E., 1965. Erosion and deposition of cohesive soils. Journal of the Hydraulics
585 Division Proceedings of the ASCE 91 (HY1), 105–139.

586 Pethick, J. S. (1980). Velocity surges and asymmetry in tidal channels. Estuarine and Coastal
587 Marine Science, 11(3), 331-345.

588 Postma, H., 1967. Sediment transport and sedimentation in the estuarine environment. In: Lauff,
589 G.H. (Ed.), Estuaries. American Association for the Advancement of Science, pp. 158–179.

590 Ren, M.E., Zhang, R.S., Yang, J.H., 1985. Effect of typhoon no. 8114 on coastal morphology and
591 sedimentation of Jiangsu Province PRC. Journal of Coastal Research 1 (1), 21–28.

592 Ren, M.E., 1986. Tidal mud flat. In: Ren, M.E. (Ed.), Modern Sedimentation in the Coastal and
593 Nearshore Zones of China. China Ocean Press, Beijing, pp. 78–127.

594 Salehi, M., K. Strom (2012), Measurement of critical shear stress of mud mixtures in the San
595 Jacinto estuary under different wave and current combinations, Cont. Shelf Res., 47, 78-92,
596 doi: 10.1016/j.csr.2012.07.004.

597 Shi, B.W., Yang, S. L., Wang, Y.P., Yu, Q., Li, M.L. 2014. Intratidal erosion and deposition rates
598 inferred from field observations of hydrodynamic and sedimentary processes: A case study of
599 a mudflat–saltmarsh transition at the Yangtze delta front. Continental Shelf Research. DIO:
600 10.1016/j.csr.2014.01.019.

601 Shi, B.W., Y.P. Wang, Y. Yang, M.L. Li, P. Li, W.F. Ni, J.H. Gao. 2015. Determination of critical
602 shear stresses for erosion and deposition based on in situ measurements of currents and

603 waves over an intertidal mudflat, *J. Coastal Res*, 31, 1344-1356.

604 Shi, B.W., Y.P. Wang, X.Q. Du, J.R. Cooper, P. Li, M.L. Li, Y. Yang. 2016. Field and theoretical
605 investigation of sediment mass fluxes on an accretional coastal mudflat. *J.*
606 *Hydro-environment Res*, 11, 75–90.

607 Shi, B.W., Cooper, J. R., Pratolongo, P. D., Gao, S., Bouma, T. J., Li, G., Li, C., Yang, S.L., Wang,
608 Y.P. 2017. Erosion and accretion on a mudflat: the Importance of very shallow-water
609 effects. *Journal of Geophysical Research: Oceans*, 122(12), 9476-9499.

610 Shields, A. (1936). Application of similarity principles and turbulence research to bed-load
611 movement. *MittPreuss. Versuchsanstalt Wasserbau Schiffbau* 26, 5–24.

612 Shields, A. (1936). Application of similarity principles and turbulence research to bedload
613 movement. *Hydrodynamic Lab. Rep. 167*, California Institute of Technology, Pasadena,
614 Calif.

615 Soulsby, R.L., Dyer, K.R., 1981. The form of the near-bed velocity profile in a tidally accelerating
616 flow. *Journal of Geophysical Research* 86 (C9), 8067–8074.

617 Soulsby R., 1997. *Dynamics of marine sands: a manual for practical applications*. Thomas Telford

618 Suykerbuyk, W., Bouma, T. J., Govers, L. L., Giesen, K., de Jong, D. J., Herman, P., van Katwijk,
619 M. M. (2016). Surviving in changing seascapes: Sediment dynamics as bottleneck for
620 long-term seagrass presence. *Ecosystems*, 19(2), 296-310.

621 van Rijn, L. C. (1993). *Principles of sediment transport in rivers, estuaries and coastal seas* (2.7,
622 2.15–2.16 pp.). Amsterdam, the Netherlands: Aqua Publication.

623 Wang, X., Ke, X., 1997. Grain-size characteristics of the extant tidal flat sediments along the
624 Jiangsu coast, China. *Sedimentary Geology*, 112(1), 105–122.

625 Wang, A.J., X. Ye, X.Q. Du, B.X. Zheng (2014), Observations of cohesive sediment behaviors in
626 the muddy area of the northern Taiwan Strait, China, *Cont. Shelf Res.*, 90, 60-69.

627 Wang, Y. P., Zhang, R., & Gao, S. (1999). Velocity variations in salt marsh creeks, Jiangsu,
628 China. *Journal of Coastal Research*, 15(2), 471-477.

629 Wang, Y. P., Gao, S., Jia, J., Thompson, C. E., Gao, J., Yang, Y. (2012). Sediment transport over an
630 accretional intertidal flat with influences of reclamation, Jiangsu coast, China. *Marine
631 Geology*, 291-294, 147-161.

632 Williams, J.J., Carling, P.A., Amos, C.L., Thompson, C., 2008. Field investigation of ridge-runnel
633 dynamics on an intertidal mudflat. *Estuar. Coast. Shelf Sci.* 79(2), 213–229.
634 <http://dx.doi.org/10.1016/j.ecss.2008.04.001>.

635 Winterwerp, J.C., and W.G.M. van Kesteren (2004), Introduction to the physics of cohesive
636 sediment in the marine environment. Elsevier, Amsterdam.

637 Whitehouse, R., Soulsby, R., Roberts, W. and Mitchener, H., 2000. Dynamics of estuarine muds:
638 A manual for practical applications. Tomas Telford Limited, Heron Quay, London.

639 Wolman, M. G., Miller, J. P. 1960. Magnitude and frequency of forces in geomorphic processes.
640 *The Journal of Geology*, 68(1), 54-74.

641 Xing, F., Wang, Y. P., Wang, H. V. 2012. Tidal hydrodynamics and fine-grained sediment
642 transport on the radial sand ridge system in the southern Yellow Sea. *Marine Geology*, 291,
643 192–210.

644 Yang, Y., Wang, Y. P., Gao, S., Wang, X. H., Shi, B. W., Zhou, L., Wang, D.D., Dai, C., Li, G.C.
645 2016a. Sediment resuspension in tidally dominated coastal environments: new insights into
646 the threshold for initial movement. *Ocean Dynamics*, 66(3), 401-417.

647 Ysebaert, T., P.M.J. Herman, P. Meire, J. Craeymeersch, H. Verbeek, C.H.R. Heip (2003),
648 Large-scale spatial patterns in estuaries: estuarine macrobenthic communities in the Schelde
649 estuary, NW-Europe, *Estuarine Coastal Shelf Sci.*, 57, 335-355, doi:
650 10.1016/S0272-7714(02)00359-1.

651 Yu, Q., Wang, Y., Shi, B., Wang, Y. P., Gao, S. (2017). Physical and sedimentary processes on
652 the tidal flat of central Jiangsu Coast, China: Headland induced tidal eddies and benthic fluid
653 mud layers. *Continental Shelf Research*, 133, 26-36.

654 Zhang, H., Madsen, O. S., Sannasiraj, S. A., Chan, E. S. (2004). Hydrodynamic model with
655 wave–current interaction in coastal regions. *Estuarine, Coastal and Shelf Science*, 61(2),
656 317-324.

657 Zhang Q., Gong Z., Zhang C.K., Zhou Z., Townend I., 2016. Hydraulic and Sediment Dynamics
658 at times of Very Shallow Water on Intertidal Mudflats: The Contribution of Waves. *Journal*
659 *of Coastal Research*, 75, 507-511.

660 Zhou, Z., Olabarrieta, M., Stefanon, L., D'Alpaos, A., Carniello, L., Coco, G. (2014). A
661 comparative study of physical and numerical modeling of tidal network ontogeny. *Journal of*
662 *Geophysical Research: Earth Surface*, 119(4), 892-912.

663 Zhu, D.K., Ke, X., Gao, S., 1986. Tidal fiat sedimentation of Jiangsu coast. *J. Oceanogr. Huanghai*
664 *Bohai Seas*, 4(3): 19–27 (in Chinese with English abstract).

665

666

Table 1 Deployment and setup description of the instruments.

Instruments	Height above the bed (cm)	Measured parameters	Burst intervals (s)	Sampling frequency (Hz)	Sampling numbers each burst
ADV	20	3D turbulent velocity	300	16 Hz	4096
OBS-3A	5	Turbidity, water depth	60	1 Hz	30
SBE 26 plus	5	Water depth, wave height and period	600	4 Hz	1024
ALEC	5	2D current velocity	30	2 Hz	30

Table 2 Comparison of bed shear stress due to wave (τ_w), current (τ_c) and combined current–wave action (τ_{cw}) and suspended sediment concentration (SSC) between water depth $h < 0.2$ m (ESWS) and $h > 0.2$ m (RDWS).

Tides	Mean τ_w (N/m ²)			Mean τ_c (N/m ²)			Mean τ_{cw} (N/m ²)			Mean SSC (kg/m ³)		
	ESWS			ESWS			ESWS			ESWS		
	Flood	Ebb	RDWS	Flood	Ebb	RDWS	Flood	Ebb	RDWS	Flood	Ebb	RDWS
T1	0.08	0.06	0.09	0.64	0.07	0.12	0.70	0.03	0.13	0.56	0.27	0.30
T2	0.02	0.07	0.06	0.37	0.16	0.13	0.36	0.09	0.14	0.58	0.27	0.34
T3	0.09	0.05	0.08	0.30	0.12	0.12	0.38	0.08	0.13	0.78	0.35	0.36
T4	0.06	0.04	0.07	0.40	0.13	0.13	0.45	0.09	0.14	0.51	0.35	0.43
T5	0.01	0.04	0.06	0.40	0.08	0.13	0.40	0.04	0.13	0.80	0.34	0.37
T6	0.05	0.06	0.04	0.35	0.12	0.11	0.37	0.08	0.12	0.74	0.36	0.42
T7	0.05	0.09	0.03	0.33	0.15	0.13	0.37	0.05	0.13	0.76	0.30	0.36
T8	0.04	0.10	0.07	0.42	0.07	0.13	0.45	0.04	0.14	0.85	0.37	0.45

Table 3 Comparison of bed-level change (BLC) and duration for an entire tidal cycle, and for water depth $h < 0.2$ m (ESWS) and $h > 0.2$ m (RDWS), and their percentage (%) of duration, and the rate of BLC (mm/min).

Tides	Entire tidal cycle		ESWS				RDWS							
	Duration (min)	BLC (mm)	Duration (min)		%	BLC (mm)		Rate (mm/min)		Duration (min)	%	BLC (mm)	Rate ($\times 10^{-2}$, mm/min)	
			Flood	Ebb		Flood	Ebb	Flood	Ebb					Flood
T1	526	-5	19	32	3.6	6.1	-10.3	+11.0	-0.5	+0.3	475	90.3	-5.7	-1.0
T2	506	+3	18	28	3.6	5.5	-4.2	+11.4	-0.2	+0.4	460	90.9	-4.2	-1.0
T3	500	+2	20	35	4.0	7.0	-7.4	+11.0	-0.4	+0.3	445	89.0	-1.6	-0.4
T4	508	0	21	32	4.1	6.3	-9.4	+9.4	-0.4	+0.3	455	89.6	0.0	0.0
T5	513	0	17	31	3.3	6.0	-7.5	+14.5	-0.4	+0.5	465	90.7	-7.0	-2.0
T6	510	-5	23	33	4.5	6.5	-8.3	+4.4	-0.4	+0.1	454	89.0	-1.1	-0.2
T7	510	+3	24	34	4.7	6.7	-6.7	+6.2	-0.3	+0.2	452	88.6	+3.5	+1.0
T8	500	-3	19	31	3.8	6.2	-5.1	+5.6	-0.3	+0.2	450	90.0	-3.5	-1.0

“-” denotes erosion, and “+” denotes accretion.

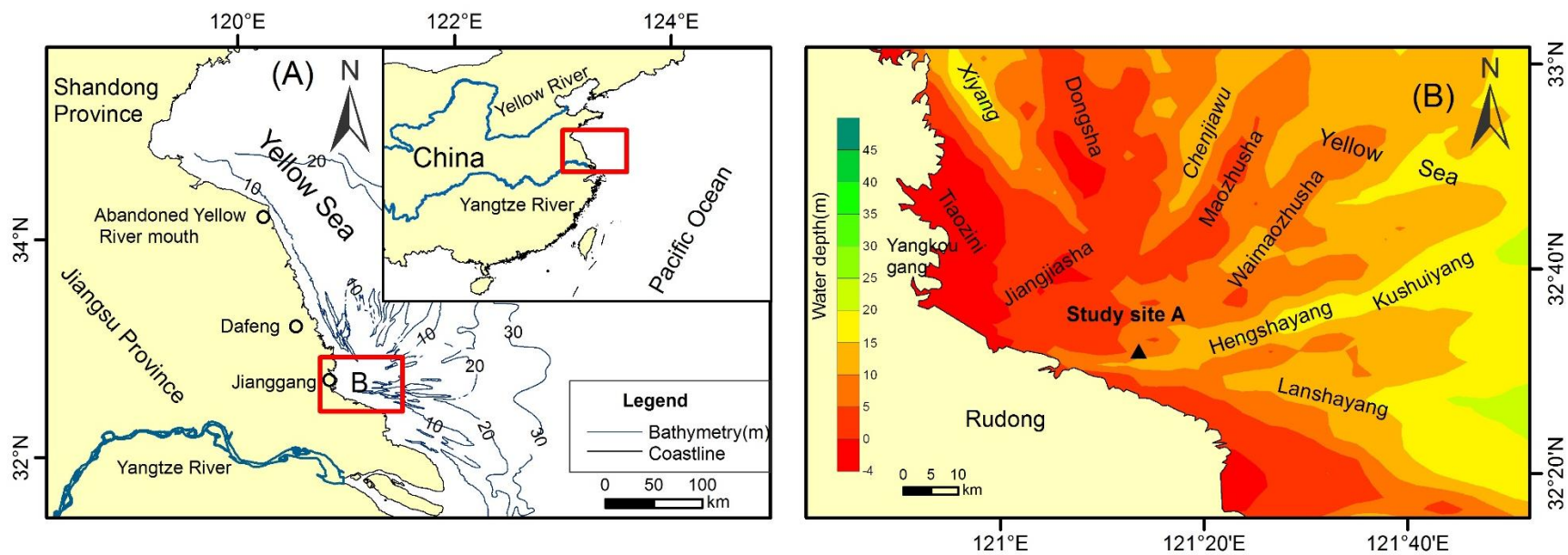


Fig. 1. Maps of the studied area. (A) Map of Jiangsu Coast and Yellow Sea, and (B) Map of Rudong intertidal flat (study site is shown by the black triangle)

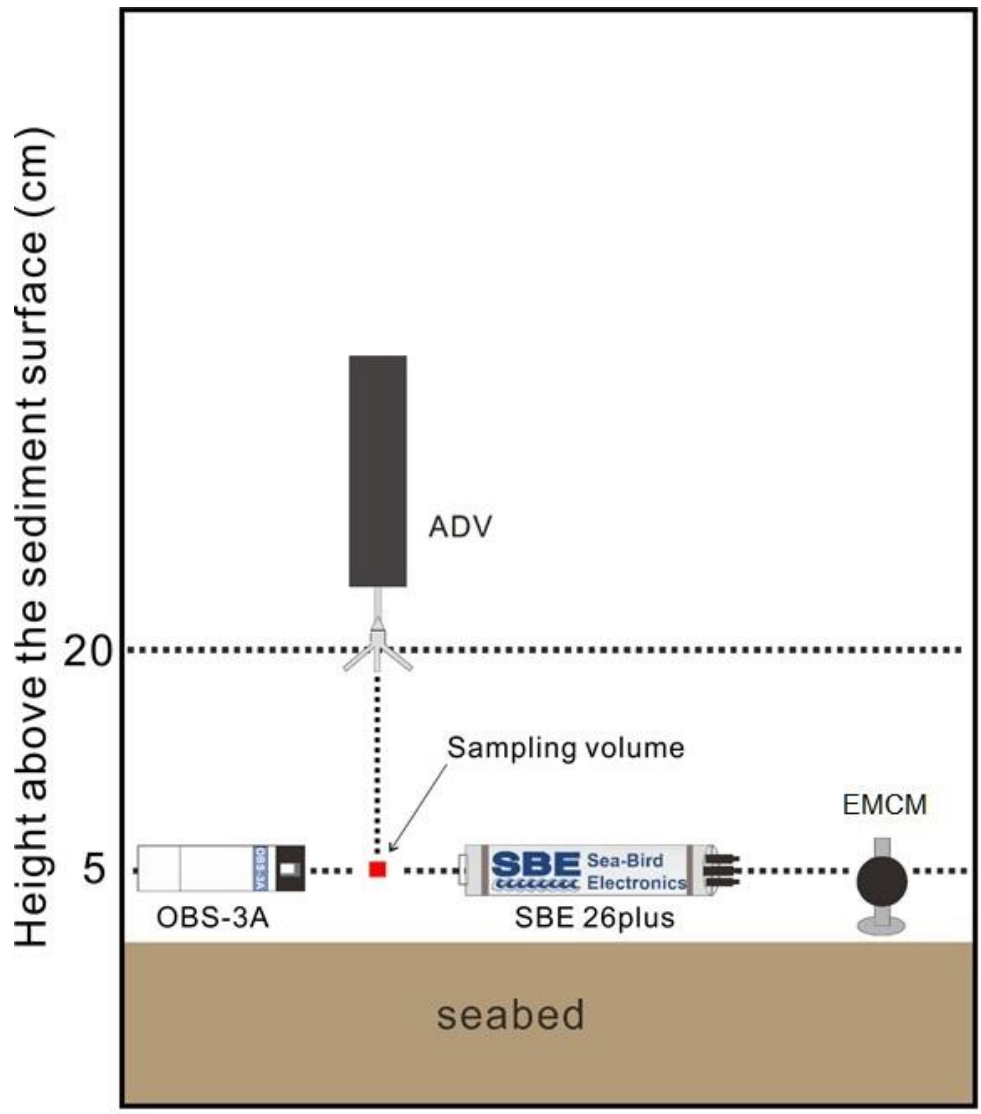


Fig.2 Schematic of the custom-made measurement frame and instrumentation.

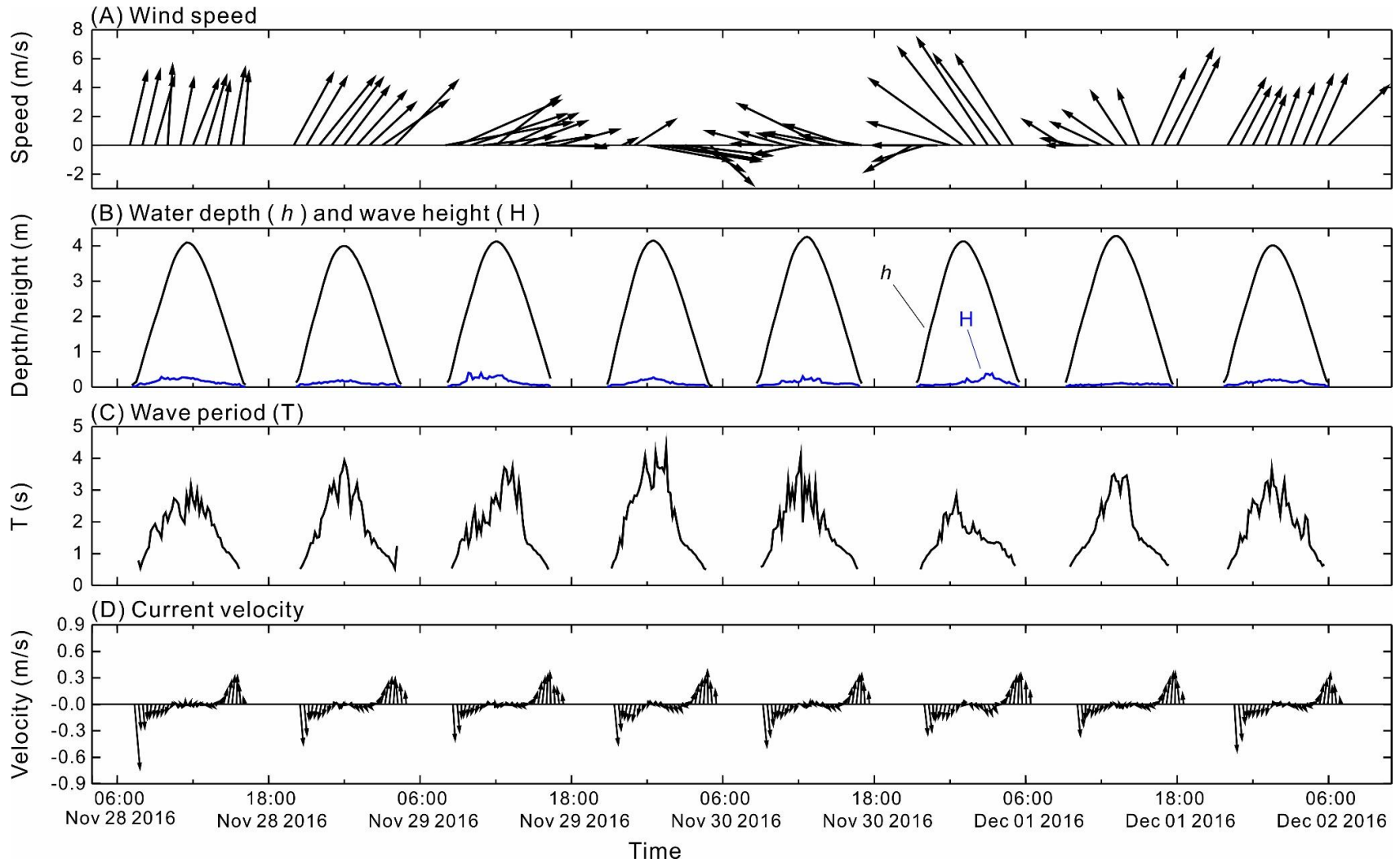


Fig.3 Time series of (A) wind speed, (B) water depth and wave height, (C) wave period and (D) current velocity during entire field measurement. No data between one tide and another indicate that instrument sensors were exposed to air and could not measure.

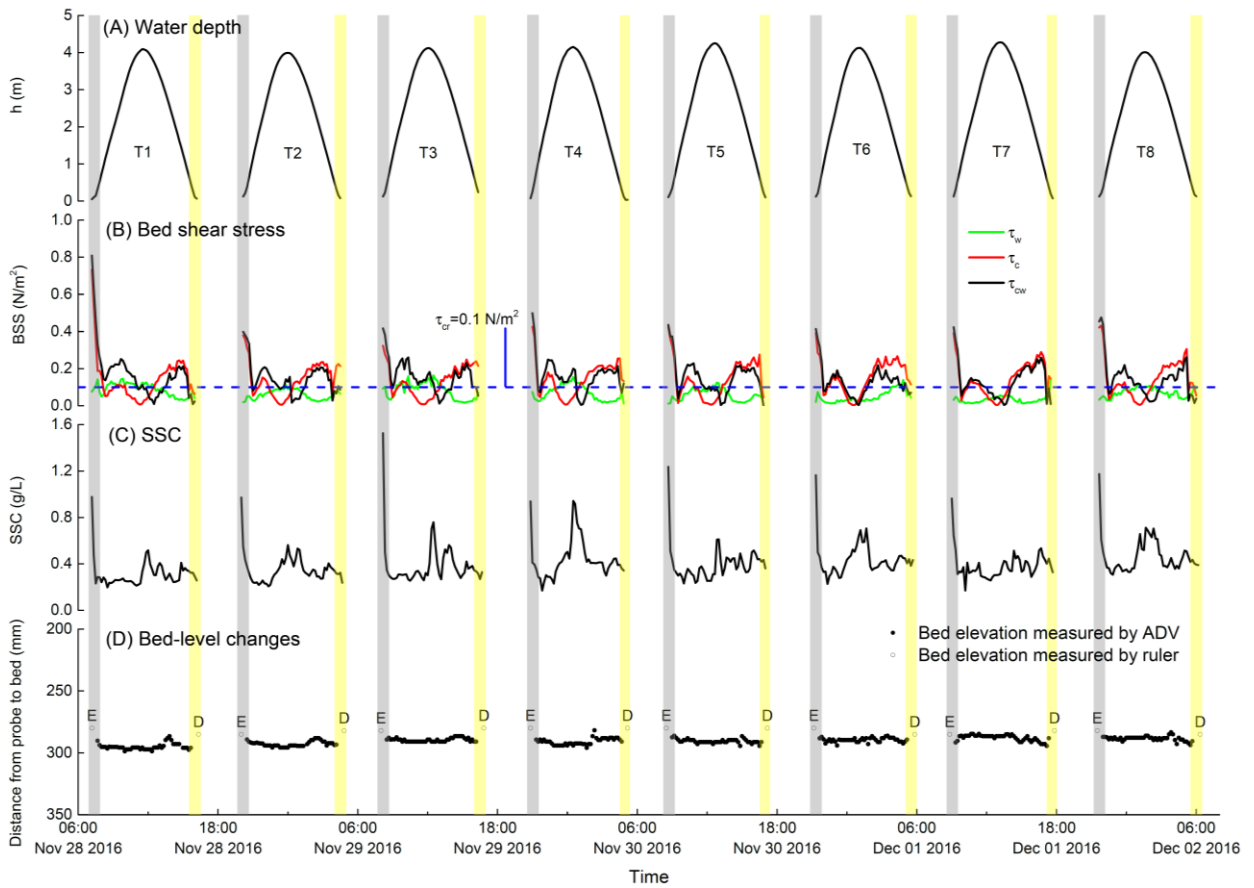


Fig.4 Time series of (A) water depth, (B) bed shear stress (τ_c , τ_w and τ_{cw}), (C) suspended sediment concentration (SSC) and (D) bed-level changes. In Fig.4B, τ_c , τ_w , τ_{cw} and τ_{cr} denote bed shear stress due to currents, waves and combined current-wave action, and critical bed shear stress for bottom sediments, respectively. In Fig.4D, gray bars identify erosion phases of ESWS at the initial flood stages (denoted by E), and yellow bars identify deposition phases of ESWS at the post ebb stages (denoted by D).